Dependence of plasmaspheric morphology on the electric field description during the recovery phase of the 17 April 2002 magnetic storm

Michael W. Liemohn,[1] Aaron J. Ridley,[1] Dennis L. Gallagher,[2] Daniel M. Ober,[3] and Janet U. Kozyra[1]

Received 24 October 2003; revised 15 December 2003; accepted 30 December 2003; published 16 March 2004.

[1] A comparison of how well three different electric field models can predict the storm time plasmapause shape is conducted. The magnetic storm of 17 April 2002 is selected for this event, and plasmapause locations are extracted from images from the EUV instrument on the Imager for Magnetopause-to-Aurora Geomagnetic Effects (IMAGE) satellite throughout the main phase and recovery phase of the event. The three electric field descriptions are as follows: the modified McIlwain E5D analytical formula, the Weimer statistical compilation from low-Earth orbit satellite data, and a self-consistent Poisson equation solution for the subauroral potential pattern. It is found that all of the models have certain strengths and weaknesses in predicting the plasmapause location during this storm. The modified McIlwain model did well on the nightside but not on the dayside because the electric fields near noon are too small (analogous to too large of a conductance in the subauroral dayside ionosphere). The Weimer model did well overall, but the resulting plasmapause is usually smaller than the observed one because the electric fields are a bit too strong in the inner magnetosphere (perhaps because of an ionosphere-magnetosphere mapping problem). The self-consistent model is also quite good in general, but the plasmapause in the postmidnight sector was always inward of the observed one. This is because of too low a conductance at the location of the field-aligned currents that close the partial ring current. It is concluded that the latter two models provide a sufficient description of the storm time development of the plasmaspheric morphology during this storm, with the self-consistent model being the best choice. Another conclusion is that plasmapause locations extracted from EUV images should be compared with peak density gradients from model results rather than with any one isocontour of the cold plasma density itself. *INDEX TERMS:* 2768 Magnetospheric Physics: Plasmasphere; 2760 Magnetospheric Physics: Plasma convection; 2712 Magnetospheric Physics: Electric fields (2411); 2788 Magnetospheric Physics: Storms and substorms; 2736 Magnetospheric Physics: Magnetosphere/ionosphere interactions; *KEYWORDS:* plasmapause location, magnetosphere-ionosphere coupling, magnetic storms

Citation: Liemohn, M. W., A. J. Ridley, D. L. Gallagher, D. M. Ober, and J. U. Kozyra (2004), Dependence of plasmaspheric morphology on the electric field description during the recovery phase of the 17 April 2002 magnetic storm, *J. Geophys. Res.*, *109*, A03209, doi:10.1029/2003JA010304.

1. Introduction

[2] The morphology of the electric field is critical to understanding the storm time inner magnetosphere. The motion of the cold plasmaspheric particles is dominated by corotation and convection electric fields, causing plasmaspheric erosion and drainage plume formation [e.g., *Chappell et al.*, 1970; *Sandel et al.*, 2003]. The cold plasma density structure, especially the location of the plasmapause, is a critical quantity that governs the efficiency of many of the wave-particle interactions in this region [e.g., *Kennel and Petschek*, 1966; *Summers et al.*, 1998]. The hot ions and electrons of the ring current are also influenced by those same two electric fields, with the additional effect of magnetic drift separating the positively and negatively charged particles [*Alfvén and Fälthammar*, 1963; *Ejiri*, 1978]. The ring current ions are the major energy carriers in the inner magnetosphere and create a diamagnetic cavity in the inner magnetosphere that alters the magnetic topology of the region [e.g., *Parker and Stewart*, 1967; *Tsyganenko et al.*, 2003]. This magnetic deformation leads to changes in the drift paths of the relativistic "radiation belt" particles, causing deenergization and/or precipitation into the upper

[1]Center for Space Environment Modeling, Atmospheric, Oceanic, and Space Sciences Department, University of Michigan, Ann Arbor, Michigan, USA.
[2]National Space Science and Technology Center, NASA Marshall Space Flight Center, Huntsville, Alabama, USA.
[3]Mission Research Corporation, Nashua, New Hampshire, USA.

0148-0227/04/2003JA010304

atmosphere [e.g., *Dessler and Karplus*, 1961; *Green and Kivelson*, 2001].

[3] Presently, there is no way of measuring the global electric potential pattern. Therefore one must rely on models to approximate the instantaneous field structure. Several such models exist and are of varying degrees of sophistication. Complexity ranges from a simple two-cell convection pattern [e.g., *Volland*, 1973; *Stern*, 1975] to statistical compilations of ionospheric data from ground-based radars [e.g., *Sojka et al.*, 1986; *Foster et al.*, 1986] or low-orbit satellites [e.g., *Papitashvili et al.*, 1994; *Weimer*, 1996] to assimilative techniques using both ground-based and satellite data [*Kamide et al.*, 1981; *Richmond and Kamide*, 1988]. Global potential patterns can also be obtained from a Poisson equation solution using model-derived field-aligned currents (FACs) [e.g., *Southwood and Wolf*, 1978; *Fok et al.*, 2001; *Ridley and Liemohn*, 2002; *Khazanov et al.*, 2003]. This last technique is referred to as the self-consistent approach because the electric fields drifting the particles in the inner magnetosphere are derived from the particle distributions themselves. All of the above-mentioned (or similar) electric field descriptions have been used extensively in the modeling of inner magnetospheric particle populations.

[4] In particular, several recent studies have explicitly compared the accuracy of various electric field models in the inner magnetosphere. *Jordanova et al.* [2001] showed that ring current simulations with the Weimer potential yielded better ion distribution comparisons against data than a Volland-Stern potential. *Boonsiriseth et al.* [2001] found that potentials from the assimilative mapping of ionospheric electrodynamics (AMIE) model [*Richmond and Kamide*, 1988], together with the penetration electric field of *Ridley and Liemohn* [2002], produced excellent agreement with in situ field electric measurements (better than the empirical models considered). Using AMIE potentials in their hot ion transport model, *Chen et al.* [2003] showed that concentrations of potential in narrow channels rapidly transport plasma sheet particles into the inner magnetosphere (a feature not found in simple two-cell models). A similar study by *Khazanov et al.* [2004a] extended these results by including the Weimer model in the comparison, finding that the morphology of that field description is in between a two-cell pattern and the AMIE fields in their complexity. Furthermore, *Khazanov et al.* [2004b] have shown that a slowly varying AMIE potential pattern is not sufficient for accuracy in the resulting plasma distributions. That is, time variability of the global potential structure is necessary to energize the injected plasma sheet particles up to hundreds of keV in energy (becoming the seed population for the radiation belts). *Fok et al.* [2001] showed that a self-consistent electric field produced a pattern significantly different from the standard two-cell morphology, in particular, the existence of an extra potential well near local midnight [cf. *Southwood and Wolf*, 1978]. *Fok et al.* [2003] then showed that this midnight potential well is capable of producing a predawn peak in the asymmetric ring current, as observed by satellite-based energetic neutral atom imagers. A follow-on study by *Khazanov et al.* [2003] showed that the potential structure is even more distorted from a two-cell pattern when self-consistent ionospheric conductances are used instead of a statistical conductance pattern. All of these results are in qualitative agreement with the strong electric fields observed in the inner magnetosphere and subauroral ionosphere during activity times [e.g., *Rowland and Wygant*, 1998; *Foster and Vo*, 2002].

[5] All of the above-mentioned comparative studies considered the influence on high-energy (that is, keV and above) particles, with the exception of *Boonsiriseth et al.* [2001], who compared against electric field data. While numerical studies of the plasmasphere over the last few decades have been conducted using a single electric field model [e.g., *Chen and Wolf*, 1972; *Lambour et al.*, 1997; *Ober et al.*, 1997; *Weiss et al.*, 1997; *Goldstein et al.*, 2002, 2003], none of these systematically compare one electric field model with another. It is useful to conduct such a study, however, because cold plasma motion is convection dominated, making it a good tracer of electric field effects.

[6] The present study follows the example of the ring current comparative studies by examining potential structure and resulting plasmaspheric morphologies for three electric field descriptions: a simple two-cell convection pattern [*McIlwain*, 1986; *Liemohn et al.*, 2001a], the *Weimer* [1996] empirical model, and a self-consistent potential model [*Ridley et al.*, 2004] driven by partial ring current FACs. The storm on 17 April 2002 is chosen for this investigation because it is a simple ''single-dip'' event caused by a shock-sheath passage ahead of a magnetic cloud (which caused a subsequent storm on 18 April).

2. Numerical Approach

[7] This study uses results from a kinetic ring current-atmosphere interaction model (RAM) that solves the gyration and bounce-averaged Boltzmann equation inside of geosynchronous orbit. Originally developed by *Fok et al.* [1993] and *Jordanova et al.* [1996], the version used here is most recently described by *Liemohn et al.* [1999, 2001a]. Using second-order accurate numerical schemes, the hot ion phase-space distribution is determined as a function of time, equatorial plane location, energy, and equatorial pitch angle, yielding a detailed description of the ring current ion population throughout near-Earth space. Sources are specified by geosynchronous orbit plasma data across the nightside outer boundary, splitting the composition for the $E < 50$ keV measurements between O^+ and H^+ according to the relations of *Young et al.* [1982] (higher-energy observations are assumed to be H^+, minus a $\kappa = 5$ high-energy extension to the lower-energy O^+ distribution). Loss mechanisms include the flow of plasma out the dayside outer boundary, precipitation of particles into the upper atmosphere, pitch angle scattering and drag from Coulomb collisions (using the plasmaspheric model of *Ober et al.* [1997]), and charge exchange with the neutral hydrogen geocorona (using the model of *Rairden et al.* [1986]). A dipole magnetic field is assumed, and an electric field description is also needed, which will be described below.

[8] The plasmaspheric model to which RAM is coupled is the dynamic global core plasma model (DGCPM) that solves a continuity equation for the total cold plasma content in a flux tube [*Ober et al.*, 1997]. The source of plasma is the dayside ionosphere, and the sink is the

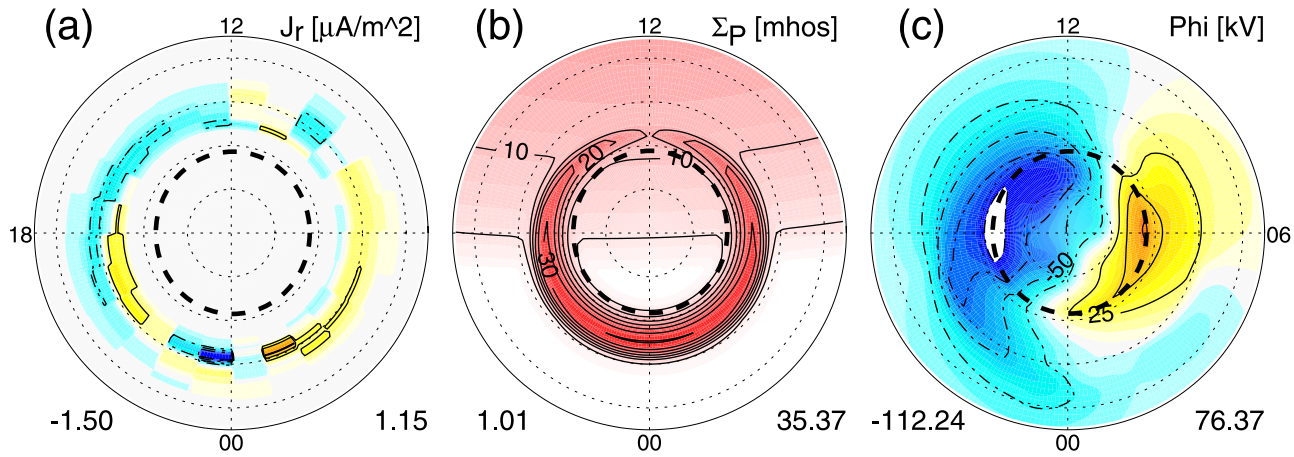

Figure 1. (a) Example field-aligned currents into and out of the ionosphere used as the source terms in the Poisson equation solution, (b) corresponding ionospheric conductance, and (c) resulting electric potential distribution. The thick black dashed circle indicates the poleward extent of the Poisson solution, with W96 potentials above this line. The view is over the North Pole onto the ionosphere in geomagnetic coordinates, with local noon to the top in each dial plot. Thin dotted circles indicate 10° increments away from the pole.

nightside ionosphere and the dayside outer simulation boundary. Equatorial densities vary between the trough densities and saturated densities from *Carpenter and Anderson* [1992] using empirically determined refilling timescales [*Chen and Wolf*, 1972; *Rasmussen et al.*, 1993]. It is a robust model that has been used to explain inner magnetospheric cold plasma observations, and details of the computational scheme are provided by *Ober et al.* [1997].

[9] Three choices for the inner magnetospheric electric field will be used. The first option is the modified *McIlwain* [1986] E5D model (as revised by *Liemohn et al.* [2001a]), which produces a skewed, variably shielded two-cell convection pattern (hereinafter option 1). The convection strength for this option is specified by the cross-polar cap potential difference ($\Delta\Phi_{PC}$) from the *Weimer* [1996] empirical model (hereinafter the W96 model). The second option is to map the W96 potential distribution into the inner magnetosphere along the dipole magnetic field (hereinafter option 2). This model is a spherical harmonic fit to low-Earth orbit satellite data and is specified by upstream solar wind conditions. The third option is a self-consistent electric field description (hereinafter option 3). The plasma phase space distributions from RAM are integrated to yield pressures, which can be converted to perpendicular currents [e.g., *Parker*, 1957], and the divergence of these currents yields FACs into and out of the ionosphere. The calculational method described by *Liemohn et al.* [2001b] is used in the present study. The FACs are used as source terms in a Poisson equation, which yields a potential distribution throughout the ionosphere. The calculation is described in more detail by *Ridley and Liemohn* [2002] and *Ridley et al.* [2001, 2004]. A high-latitude boundary condition is applied at ~72°, defined by the W96 potential distribution at that magnetic latitude. A low-latitude boundary of zero potential is applied at 30°. The ionospheric conductance is dynamically defined according to the RAM-generated FACs. It is a smooth, continuous oval in longitude with a Gaussian latitudinal profile (half width of ~4°). The latitude of the peak conductance is shifted poleward of the ring current-generated FAC peak by 5° to put the center of the oval between the RAM-calculated region 2 FACs and the higher-latitude region 1 FACs (a shift similar and opposite to that used by *Ridley et al.* [2001], whose MHD model included strong region 1 FACs but essentially no region 2 FACs). The peak magnitude is scaled by the peak FAC value as defined by *Ridley et al.* [2004]. Because the FAC-to-Σ relationship was created using region 1 FAC strengths, an extra multiplier of 5 is included in the formula to account for the nominal difference between region 1 and region 2 FAC intensities [e.g., *Iijima and Potemra*, 1976; *Weimer*, 1999]. In addition to this auroral oval conductance a dayside sunlight conductance is included along with a 1 S Pedersen conductance from starlight and scattered light ionization applied everywhere in the simulation domain (including the nightside) [e.g., *Strobel et al.*, 1974]. Figure 1 shows an example plot of input FACs from the RAM, the Pedersen conductance for this time, and the resulting electric potential. The thick black dashed circle is the high-latitude boundary of the Poisson equation solution, above which a W96 potential is used. Option 3 is similar to other self-consistent inner magnetospheric electric field calculations [*Spiro and Wolf*, 1984; *Fok et al.*, 2001; *Khazanov et al.*, 2003], with the primary difference being the chosen conductance pattern.

3. 17 April 2002

[10] At ~1155 UT on 17 April 2002 a shock in the solar wind struck the magnetosphere. The resulting magnetic storm was the first in a series occurring over the next week as at least three interplanetary coronal mass ejections passed by Earth. The present study focuses on the first shock hit and subsequent sheath passage, which lasted over 12 hours (the cloud passage began early on 18 April). This first sheath passage of the storm series produced a well-defined main phase and recovery phase, during which there are ample data for simulation input and result comparison.

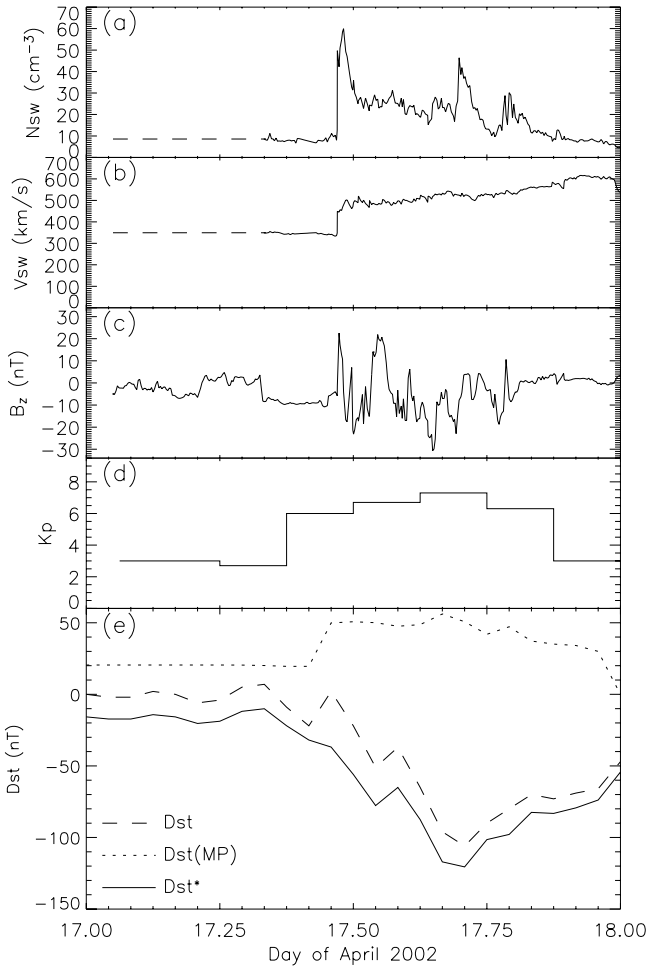

Figure 2. Solar wind and geophysical conditions on 17 April 2002: (a) solar wind density; (b) solar wind velocity $V_{x,\mathrm{GCM}}$; (c) interplanetary magnetic field $B_{z,\mathrm{GCM}}$; (d) *Kp*; and (e) *Dst* (dashed line), magnetopause contributions to *Dst* (dotted line), and *Dst** (solid line). The dashed line segments in Figures 2a and 2b show interpolated values through a data gap.

[11] Figure 2 shows the solar wind conditions (density and speed from ACE Solar Wind Electron Proton Alpha Monitor (SWEPAM) key parameter data [*McComas et al.*, 1998]), interplanetary magnetic field (IMF) (IMF B_z from ACE Magnetic Field Experiment key parameter data [*Smith et al.*, 1998]), and the geophysical response (*Kp* and *Dst* indices from the Kyoto World Data Center [*Sugiura and Kamei*, 1991]) on 17 April. The ACE data have been time shifted to the Earth by a $V_{\mathrm{GSM}}/X_{\mathrm{GSM}}$ delay. There is a large density and velocity jump when the shock hits, and both quantities remain elevated throughout the rest of the day. Large positive and negative excursions are seen in the IMF B_z until 1930 UT. This resulted in a peak *Kp* value of 7+ and a *Dst* minimum of −105 nT. Also shown in Figure 2e are the magnetopause contributions to *Dst* and *Dst** (*Dst* with removal of the magnetopause value and an induced current effect (see equation (1) of *Liemohn et al.* [2002] for the exact formula of *Dst**)). There is a SWEPAM data gap until 0800 UT (the dashed lines in Figures 2a and 2b), but this does not significantly affect the results of the present study, which focus on the second half of 17 April. Furthermore, solar wind key parameters from Wind (at $Y_{\mathrm{GSM}} \sim 200\ R_E$) and Geotail (in the magnetosheath) are consistent with steady upstream conditions for the first half of 17 April.

[12] Figure 3 shows a condensation of the input values to the RAM. Figures 3a–3c show the density, perpendicular temperature, and temperature anisotropy from nightside magnetospheric plasma analyzer (MPA) measurements (see *Liemohn et al.* [2001a] for details of the data selection criteria). Figure 3d shows the $\Delta\Phi_{\mathrm{PC}}$ time series from the W96 model. The peaks in $\Delta\Phi_{\mathrm{PC}}$ are coincident with the southward IMF B_z intervals seen in Figure 1c. Figure 3e shows the observed *Dst** time series for reference. There is an MPA data gap until 1200 UT (the dashed lines in Figures 3a–3c), but, like the solar wind data gap, filling it with a linear interpolation of the quiescent values from earlier and later times is thought to be reasonable and does not significantly affect the results of the present study.

4. Results

[13] While the focus of this study is on plasmaspheric dynamics during the 17 April 2002 magnetic storm, it is the ring current dynamics that govern the inner magnetospheric electric potential structure (a primary factor influencing the

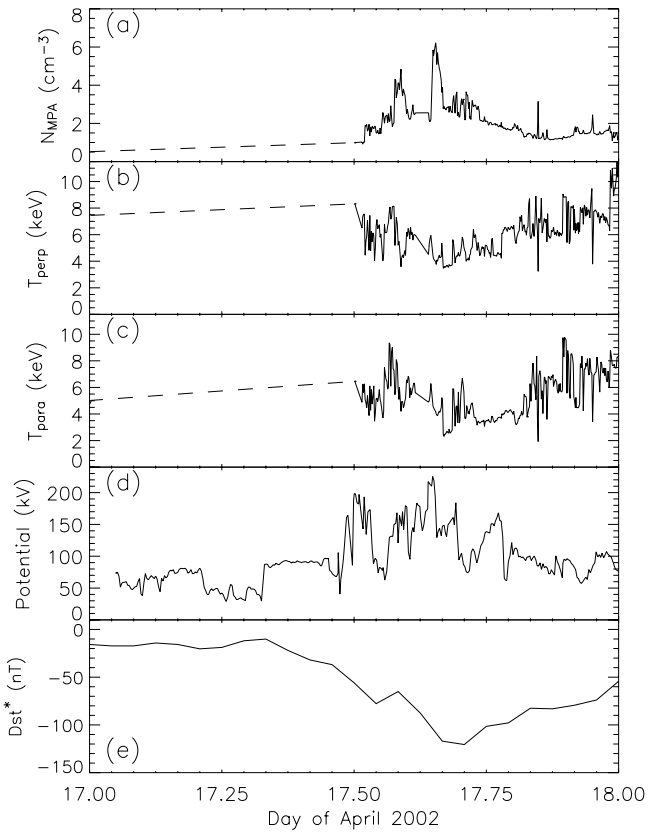

Figure 3. Input quantities to the ring current model for 17 April 2002: (a) nightside geosynchronous plasma density, (b) nightside geosynchronous perpendicular temperature, (c) nightside geosynchronous parallel temperature, (d) cross-polar cap potential (from W96), and (e) *Dst** (as in Figure 1, for reference). The dashed line segments in Figures 3a–3c show interpolated values through a data gap.

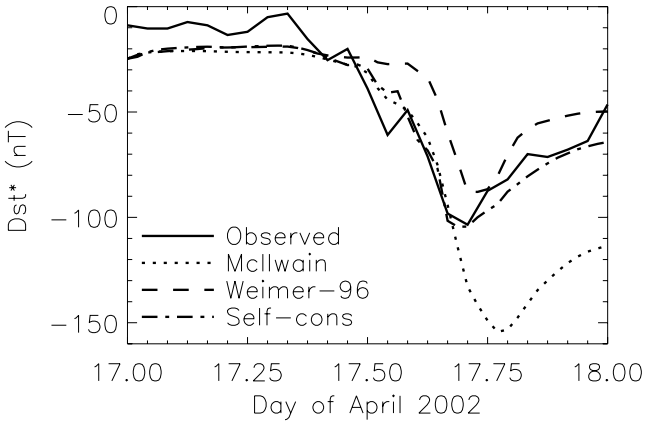

Figure 4. Observed *Dst** (solar line) and ΔB_{DPS} for the three simulations (each with a different electric field option).

plasmapause location). Therefore it is useful to begin the data-theory comparisons with an examination of the ring current results from these simulations.

[14] A crude but nonetheless valuable analysis of the ring current simulation results is to reduce the entire hot ion distribution to a single number. The Dessler-Parker-Sckopke (DPS) equation [*Dessler and Parker*, 1959; *Sckopke*, 1966] relates the total plasma energy content to the magnetic perturbation at the center of the Earth. The resulting ΔB_{DPS} time series can be directly compared against the observed *Dst** [e.g., *Greenspan and Hamilton*, 2000]. Recently, *Liemohn* [2003 and references therein] confirmed the validity of this data-theory comparison. A finding of *Liemohn* [2003] is that ΔB_{DPS} includes a crude proxy of the contribution from currents beyond the integration volume, and therefore the tail current influence on *Dst** is roughly included in this comparison.

[15] Figure 4 presents ΔB_{DPS} for simulations with the three electric field options. It is seen that electric field option 3 produces a ΔB_{DPS} time series quite close to the observed *Dst** time series. The simulation using option 1 matched the main phase of the storm quite well, but the peak perturbation is overestimated by 50%, so the recovery phase is completely off. The simulation using option 2 begins the main phase later than observed, yielding a smaller total perturbation, and the shape of its *Dst** curve during the recovery phase is different than observed.

[16] For the plasmaspheric data-theory comparisons, observations from the EUV instrument [*Sandel et al.*, 2000] on the Imager for Magnetopause-to-Aurora Geomagnetic Effects (IMAGE) spacecraft [*Burch*, 2000] are employed. This camera records snapshots of the HeII 30.4 nm light resonantly scattered off of helium ions. It is quite effective at seeing the fluorescence of the He^+ in the plasmasphere, and small-scale features in the plasmapause (the relatively sharp outer boundary of the plasmasphere) are discernible from the images. Figure 5 shows the IMAGE orbit projection in the X_{SM}-Z_{SM} plane. The spacecraft is always within 1.5 R_E of the Y_{SM} = 0 axis, with apogee (~1700 UT) slightly premidnight (within half an hour local time) and perigee (~0000 UT) slightly prenoon. The EUV instrument collects data only during the high-latitude portion of the orbit, and observations begin at 1550 UT and end at 2240 UT on this pass.

[17] Figure 6 (top) presents four EUV images from the 17 April 2002 storm. During the storm, IMAGE was ascending toward apogee during the main phase and descending toward perigee during the recovery phase. Therefore the view in the EUV images of Figure 6 is over the North Pole with the Sun-Earth line 16° below horizontal to the left. A Sun-blocking shutter prevents dayside observations during the main phase (first image), but the nightside plasmasphere (and plasmapause drop-off in intensity) is visible. Continuing into the recovery phase of the storm, the shutter blocks progressively less of the view around Earth, and the dayside plasmasphere comes into view.

[18] Because the measurements are line-of-sight integrals of the emissions, a deconvolution is necessary to convert the data into a useful geophysical quantity. A relatively simple technique is to map the images into the equatorial plane, assuming that most of the observed photons are coming from the equatorial region. A plasmapause location as a function of radial distance in the equatorial plane (R) and magnetic local time (MLT) can then be extracted from the converted image. These EUV-derived plasmapause locations are shown in the bottom row of plots in Figure 6, overlaid as circles on top of DGCPM cold plasma density results from the option 3 electric field simulation. It is seen that the general shape of the plasmapause is qualitatively similar, but nothing quantitative can be concluded from this comparison. Therefore only one simulation result is shown

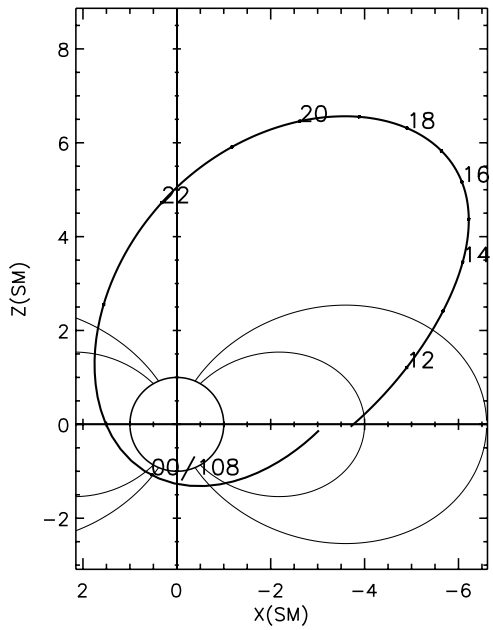

Figure 5. Imager for Magnetopause-to-Aurora Geomagnetic Effects (IMAGE) orbit projection in the X_{SM}-Z_{SM} plane from 1100 UT on 17 April 2002 to 0100 UT on 18 April 2002. Axis distances are in Earth radii, and the numbers listed on the plot are UT hours. The orbit plane is offset very slightly westward from the noon-midnight meridian.

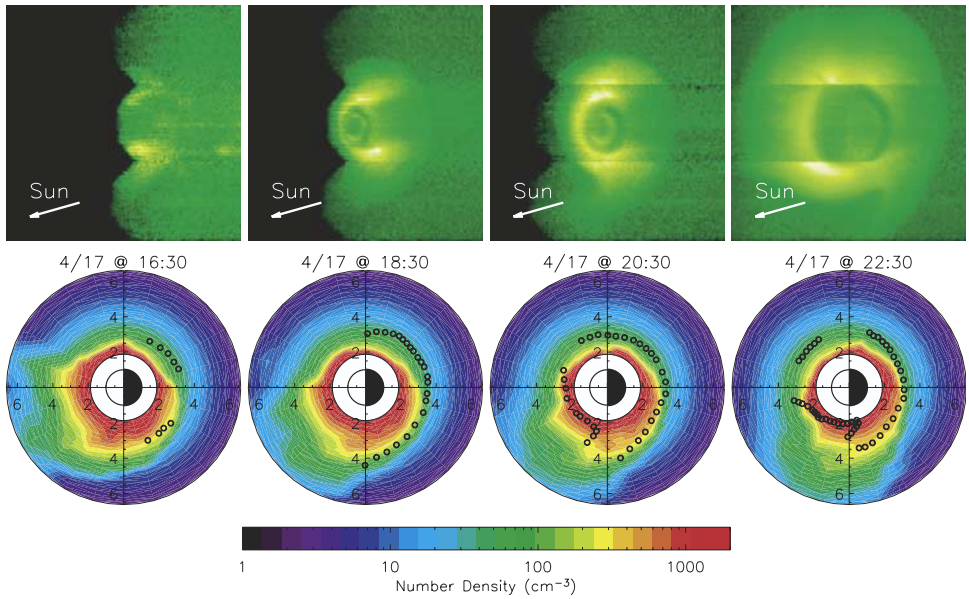

Figure 6. EUV images at UT = 1630, 1830, 2030, and 2230 on 17 April 2002 and corresponding modeled plasmaspheric equatorial densities. In the EUV images the view is over the North Pole with the Sun off to the left and slightly downward, as indicated. In the model results the view is over the North Pole with the Sun directly to the left, and distances are given in Earth radii. The circles are plasmapause locations extracted from the EUV images.

in this format, and a more suitable data-theory comparison method is used henceforth.

[19] The values taken from the IMAGE EUV data are plasmapause locations, and therefore it is more illustrative to compare these values against the gradient of the DGCPM density results (rather than the density itself). The technique of using the density gradient to identify the plasmapause location was first used by *Carpenter* [1963], who discovered the "knee" in the cold plasma density from whistler data. Figure 7 shows this comparison for the three electric field options (the three rows) and the four times (the four columns) shown in Figure 6. As in Figure 6 the EUV-derived plasmapause locations are overlaid as circles on each plot. To compute the gradient, the logarithm (base 10) of each equatorial density value was taken, and then the gradient (derivatives in both radial and azimuthal directions) was found, normalizing the values into units of per Earth radius. Colors in the purple to blue range indicate a small gradient in the density, while colors in the yellow to red range show places with very large gradients. The choppiness of the color is a plotting artifact from undersampling the computational array for the output file and is not geophysically meaningful.

[20] Because the plasmapause location is dependent on the inner magnetospheric electric field structure (and time history), it is useful to present the electric potentials for each of the field options. Equipotential contours are shown in Figure 8. Each dial plot is the result for the same model choice and time as the corresponding subplot in Figure 7. Each color gradation is separated by ~7.5 kV. Note that the corotation potential is not included in Figure 8. It would appear as a 92 kV potential well centered on the Earth, dropping off as per Earth radius. Therefore it dominates near the Earth but diminishes in efficacy away from the Earth. During storm conditions the transition between corotation dominance and convection dominance can be inside of $R = 4\ R_E$, while during quiet times this transition is often beyond geosynchronous orbit.

[21] From the density gradient plots in Figure 7 the location of the plasmapause in the simulation results can be determined quantitatively. The simulated plasmapause location is defined as the radial distance of the peak density gradient for each MLT. An analysis of the goodness of the model results can now be performed. Figure 9 shows the root-mean-square (RMS) error between the DGCPM-derived plasmapause locations and the EUV-derived plasmapause locations (at the MLTs of the EUV values), computed every 30 min throughout the event. The RMS errors in five different MLT ranges are shown in Figure 9 for each 6-hour quadrant around the Earth and all 24 hours of magnetic local time. Note that some of the sectors (namely, those on the dayside) start later in universal times than others because of the Sun-blocking shutter on the EUV camera.

5. Discussion

[22] Let us now interpret the results presented in section 4. From the $\Delta B_{\mathrm{DPS}} - Dst^*$ comparisons shown in Figure 4, it appears that option 3 is the best of the three electric field descriptions for defining the storm time ring current during this event. Note that Dst^* is only a rough estimate of the ring current strength, and therefore this is merely a qualitative assessment. It is useful, however, because the ring current intensity is a critical factor in the inner magnetospheric potential morphology (when computed self-consistently). The results shown in Figure 4 provide a context for the subsequent plasmaspheric results.

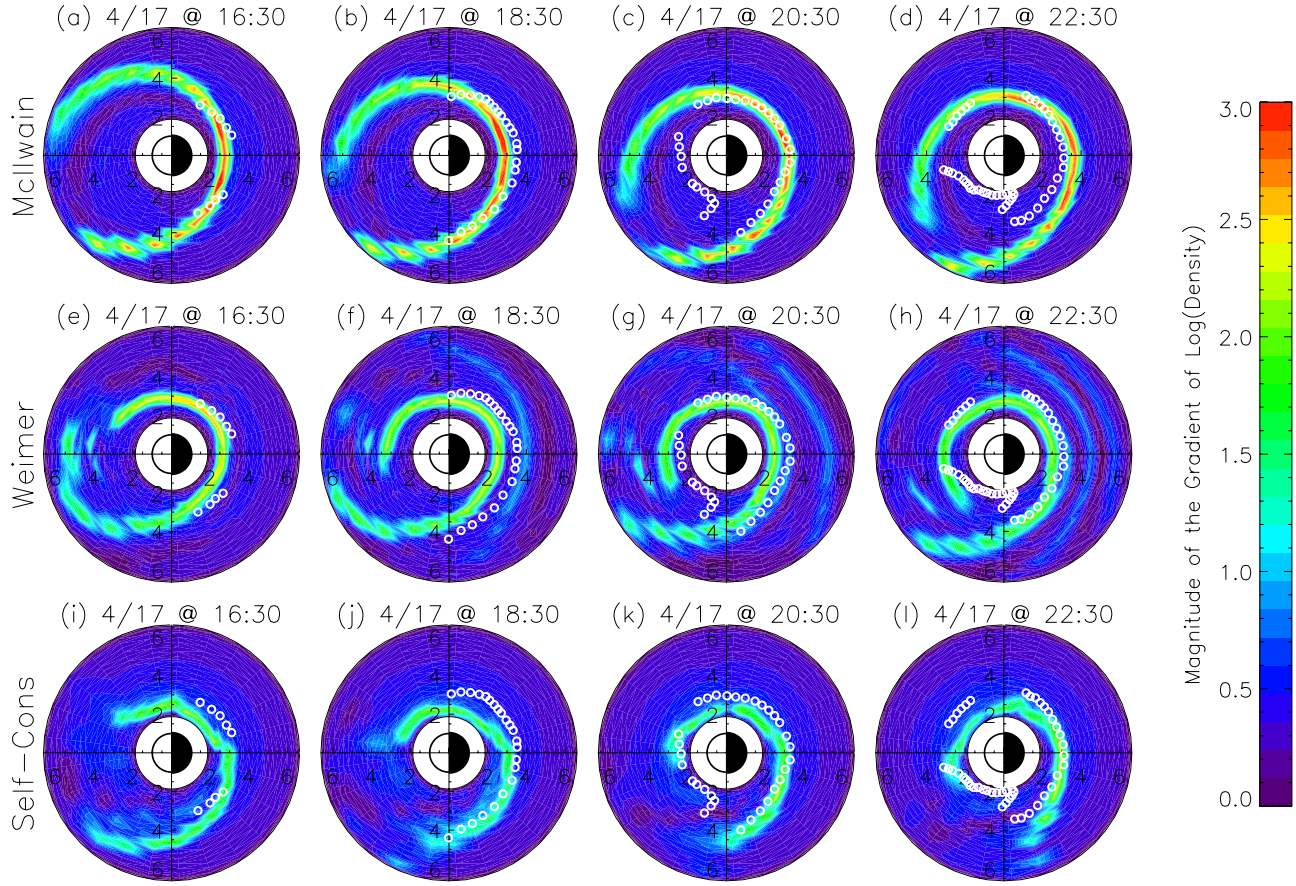

Figure 7. The magnitude of the gradient in plasmaspheric density for the three simulations (the three rows) at the four times shown in Figure 6 (the four columns). The circles are the plasmapause locations extracted from the EUV images.

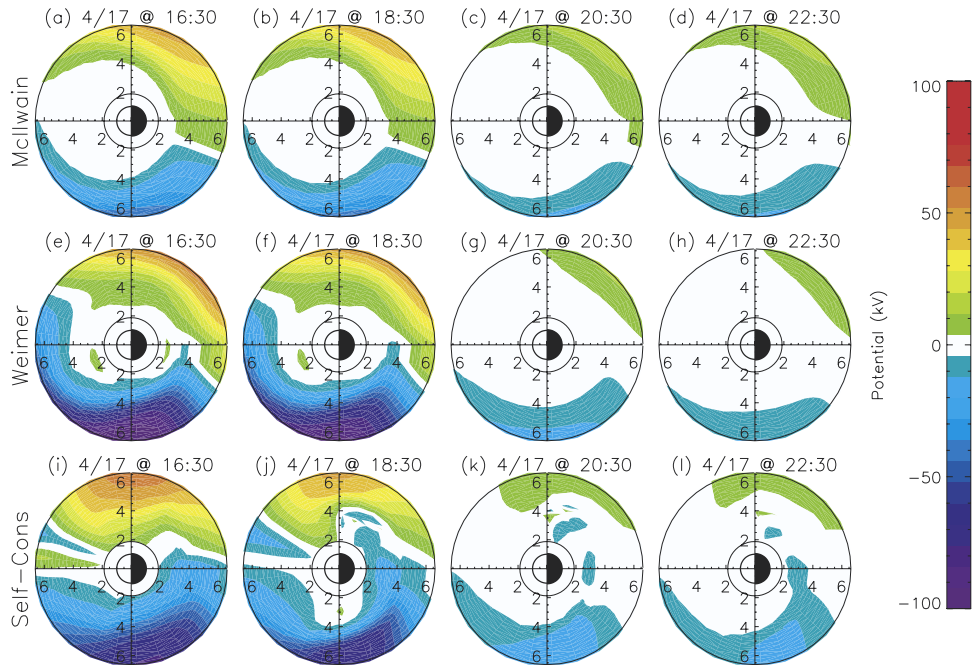

Figure 8. Inner magnetospheric potential patterns from the three simulations (the three rows) at the times (the four columns) shown in Figure 7.

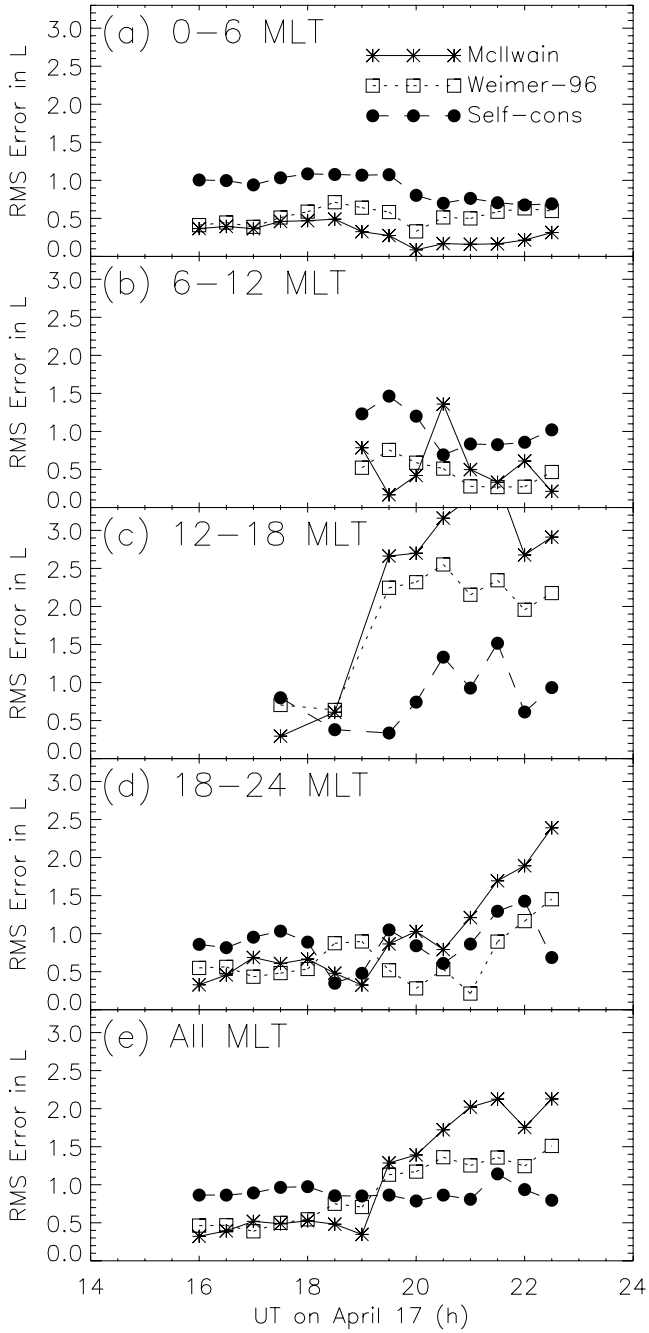

Figure 9. Root-mean-square errors between the EUV-derived plasmapause location (R) values and the model-derived plasmapause R values. The results are shown for (a–d) each local time quadrant and (e) all local times. The three simulations are shown as the three line styles in each plot.

[23] The bottom row of Figure 6 illustrates one of the results of this study: It is difficult to compare plasmapause locations extracted from EUV images with a particular cold plasma density isocontour. That is, the sharp boundary seen in the images does not necessarily correspond to any single plasmaspheric density level. This seems obvious when one considers the statistically derived R dependence of the plasmaspheric equatorial density (and the plasma trough) [e.g., *Grebowsky et al.*, 1974; *Carpenter and Anderson*, 1992; *Gallagher et al.*, 1995, 1998], as well as the nonlinear R dependence of the He^+ concentration in the plasmasphere [*Craven et al.*, 1997; *Gallagher et al.*, 2000]. The lack of clarity in the data-model comparisons shown in Figure 6, especially considering the higher clarity in Figure 7, implies that the EUV images provide a good estimate of the relative density but are not an absolute value (without additional data processing).

[24] Therefore let us move to a discussion of the features seen in the DGCPM results of Figure 7. The top row (option 1) shows a well-defined "tear drop" plasmapause (at all four UTs). The dusk-emanating plasmaspheric plume in the EUV-derived plasmapause locations is not created by this electric field description. The reason for this is seen in the potential patterns shown in Figure 8. The McIlwain E5D model has a strongly shielded dayside inner magnetosphere, with very little convection potential in this region. This lack of dayside potential gradients is analogous to a high dayside (particularly subauroral) conductance, which suppresses the electric fields there. In comparing the top row with the bottom row (the self-consistent potentials), it is seen that this suppression is overestimated. The nightside penetration of the electric potential from option 1 brings the region of strong electric fields in quite close to the Earth. This appears to be correct because the DGCPM plasmapause shape is very close to the observed one.

[25] The middle row of Figure 7 (option 2) does include the low-density trough in the afternoon sector between the plasmasphere and the plume. This can be understood by considering the potential patterns in the middle row of Figure 8. The W96 model produces large electric fields in the afternoon sector, and the plasmasphere is rapidly convected out of the simulation domain. In the recovery phase, convection nearly ceases, and the corotation potential (not shown in these plots) dominates the motion of the eroded plasmasphere and its plume. The DGCPM plasmapauses appear to be quite similar to the EUV-derived plasmapauses, except that there is a systematic inward offset to the numerical results at most MLTs. A caveat to the interpretation of the W96 potentials shown in Figure 8 is that a dipole magnetic field was used for the ionosphere-magnetosphere mapping. This is not correct during magnetic storms [e.g., *Tsyganenko et al.*, 2003], particularly at the larger radial distances (say, out near geosynchronous orbit). To minimize the errors associated with this magnetic field choice, a rather modest storm event was selected for this study (see the *Dst* values in Figures 1 and 4). The consequence of using a dipole instead of a stretched magnetic field is that the inner magnetospheric electric fields are perhaps overestimated, and therefore the plasma drifts might be larger than they should be. A stretched magnetic field would most likely decrease the convection strength in the simulation domain and therefore would correct some (or all) of the systematic inward offset in plasmapause location.

[26] The third row of Figure 7 (option 3) is, in general, quite similar to the option 2 results. One clear difference is that the plume is skewed more toward the nightside in the option 3 results, putting it closer in line with the observed plasmapause position. However, in the postmidnight sector the plasmapause from field option 3 is systematically inward of the EUV-derived location. This is understood

Table 1. Ratios of the Duskside-to-Dawnside Inner Magnetospheric Potential Difference

E Field Option	1630 UT	1830 UT	2030 UT	2230 UT
1	0.92	0.91	0.86	0.90
2	1.82	1.85	1.18	1.31
3	1.35	1.53	2.16	2.15

by considering the bottom row of Figure 8. This electric potential description produces a potential well near midnight. This is from the closure of the partial ring current, the mechanism responsible for subauroral polarization streams [e.g., *Foster and Rich*, 1998; *Ridley and Liemohn*, 2002]. The result is a strong westward electric field in the postmidnight region, which forces the plasmasphere inward in this region. The systematic offset with the observations indicates that this westward electric field is too large in the simulation. Because the auroral conductance peak is shifted poleward of the FAC peak at all MLTs, the conductance is underestimated in this region, where the drift of electrons should bring them closer to the Earth than the ions are. This error in plasmapause location then corotates into the prenoon sector, causing this region to also be affected. Even though the midnight potential well is the cause of this systematic error, it is a real and necessary feature. It persists into the recovery phase, influencing the location of the plasmaspheric plume (especially its nightside edge) and giving option 3 a good fit to the data in the premidnight sector.

[27] The qualitative analysis of Figures 7 and 8, however, does not clarify which electric field model has the best data-theory comparison, and a quantitative examination of these plasmapause differences is needed. Thus Figure 9 shows the essential results of this study. In Figure 9a it is seen that the option 1 run is best at all UTs during the event. The reason for this is seen in the potential patterns shown in Figure 8. Like the self-consistent potentials, the W96 potential patterns also include the midnight potential well, albeit much smaller (diminished by the statistical averaging). The stronger electric fields close to the Earth in options 2 and 3 cause the plasmapause to be incorrectly located in the postmidnight sector. Note, however, that the difference is on the order of 1 R_E or less for all three simulations.

[28] In the morning sector (Figure 9b), option 2 usually provides the best fit, while option 1 is also often quite good. The error with option 3 is due to the postmidnight electric field issue and is therefore an explainable (and correctable) error. As in Figure 9a the errors are usually less than 1 R_E, with a few RMS error values up near 1.5 R_E.

[29] Figure 9c shows the afternoon comparisons. Here it is clear that the option 3 results are better than the other two results. Option 3 has RMS errors that are always less than 1.5 R_E, while the other two field models are above 2 R_E for most of the recovery phase. Note that the first two UT comparisons, when all of the models are reasonably good, are based on only one or two data points in this sector.

[30] Figure 9d (premidnight sector) is a complicated plot. All three field options are reasonably good (less than 1 R_E error) up to 2000 UT, and then they all get progressively worse with time. In this latter period the plume is rotating into this MLT region. It is seen that options 2 and 3 trade off as the best fit to the data, while both are better than option 1 throughout this interval.

[31] Figure 9e shows the RMS errors for all MLTs together. A very clear conclusion can be drawn from this plot. During the main phase of the storm, when EUV was only observing the nightside plasmasphere, the ordering of the data-theory comparisons is as follows: Options 1 and 2 are about equally good, with option 3 slightly worse but still at or below 1 R_E of error. During the recovery phase of the storm, when EUV was observing progressively more of the dayside plasmasphere, the ordering is like this: option 3 is best with an error around 1 R_E, option 2 is next with an error approaching 1.5 R_E, and option 1 is third best with an RMS error growing to more than 2 R_E. Because the source of the nightside differences in the option 3 results has been identified and is correctable, these results imply that a self-consistent electric field is best at reproducing the observed storm time plasmapause shape (of the three models considered, for this particular magnetic storm).

[32] A comparison of Figures 9a and 9b against 9c and 9d reveals that, in general, the selected electric field models are better on the dawnside than on the duskside during the 17 April 2002 magnetic storm. This is primarily because of the presence of the plume on the duskside of the Earth, and its position is rather sensitive to the time history of the electric field in this region. However, it highlights the issue of the dawn-dusk asymmetry in the potential pattern [e.g., *Lu et al.*, 1989; *Boonsiriseth et al.*, 2001]. For instance, *Lu et al.* [1989] found that the duskside potential difference is typically 1.5 times larger than the size of the dawnside potential difference. Table 1 summarizes the ratios of the duskside-to-dawnside potential differences for the 12 panels of Figure 8. Note that the potential differences are those across the inner magnetosphere, i.e., from the Earth out to a distance of 7 R_E in the equatorial plane. Table 1 shows that electric field option 1 has a rather constant ratio of $\sim$0.9, much less than the empirically derived value of 1.5. It is therefore not surprising that the modeled duskside plasmapause location is well outside of the observed plasmapause in this region (throughout the storm). Option 2 is greater than 1.5 during the main phase of the storm but then drops below 1.5 during the recovery phase. This difference is evidenced in the errors between the observed and modeled plasmapause locations. During the main phase, option 2 yields an inward offset for the duskside plasmapause, while in the recovery phase the offset is reversed. Option 3 has values in the neighborhood of 1.5 during the main phase but then very large ratios during the recovery phase. Interestingly, this option yields the best comparison with the duskside plasmapause observations. These results indicate that a duskside-to-dawnside potential ratio of $\sim$1.5 during the main phase of the storm is more important for good data-model comparisons than a similar potential ratio at other times during the event. That is, this potential ratio matters when the potentials are large.

6. Conclusions

[33] A comparative study was undertaken to examine the strengths and weaknesses of three different electric field models at reproducing the plasmaspheric morphology during the magnetic storm on 17 April 2002. It was found that the modified McIlwain E5D model [*McIlwain*, 1986; *Liemohn et al.*, 2001a] is good at predicting the nightside plasmapause location, particularly in the post-

midnight sector. However, the small electric fields on the dayside from this model yield incorrect dayside morphologies for the storm time plasmasphere, at least during the recovery phase of the storm. This also results in a systematically larger ring current energy content than was observed (as defined by *Dst**). The *Weimer* [1996] electric field model yields a better dayside description of the plasmapause, particularly regarding the shape of the plasmaspheric plume relative to that produced by the modified McIlwain description. The electric fields are somewhat too strong in the inner magnetosphere, though, resulting in a systematically smaller plasmasphere than the plasmasphere extracted from the observations (and a smaller ΔB_{DPS} than the observed *Dst**). The third electric field model is a self-consistent algorithm that uses the FACs from the storm time partial ring current as source terms in a Poisson equation solution for the subauroral potential structure (including a dynamically defined ionospheric conductance) [*Ridley and Liemohn*, 2002; *Ridley et al.*, 2004]. This choice yielded the best comparison with the observed plasmaspheric plume location. The only caveat to this conclusion is that a systemic error of too low a conductance in the postmidnight region led to a modeled plasmapause that was inward of that observed in this MLT quadrant.

[34] While none of the models was perfect, it appears that either a *Weimer* [1996] electric field or a self-consistent electric field is sufficient to describe the temporal development of the plasmapause. This is similar to the conclusion reached in comparative electric field studies of the hot plasma distribution [e.g., *Jordanova et al.*, 2001; *Fok et al.*, 2001, 2003]. The modified McIlwain model was not particularly good at reproducing the observed dayside/duskside plasmapause shape in the recovery phase of the storm. It is believed that a self-consistent electric field would yield an even better description of storm time plasmaspheric morphology once the known deficiencies with the ionospheric conductance choice (especially a tilt to make the latitude of the conductance peak asymmetric in local time) are corrected. A full parametric study of the influence of ionospheric conductance on plasma distributions in the inner magnetosphere is recommended as the logical next step to this work.

[35] **Acknowledgments.** The authors would like to thank the sources of funding for this study: NASA grants NAG5-10297 and NAG-10850 and NSF grant ATM-0090165. The authors would like to thank all of their data providers who made the ring current simulations possible, especially M. F. Thomsen and G. D. Reeves at the Los Alamos National Laboratory, the Kyoto World Data Center for the *Kp* and *Dst* index, and CDAWeb for allowing access to the plasma and magnetic field data of the ACE spacecraft.

[36] Arthur Richmond thanks Mei-Ching Fok and another reviewer for their assistance in evaluating this paper.

References

Alfvén, H., and C.-G. Fälthammar (1963), *Cosmical Electrodynamics*, Oxford Univ. Press, New York.

Boonsiriseth, A., R. M. Thorne, G. Lu, V. K. Jordanova, M. F. Thomsen, D. M. Ober, and A. J. Ridley (2001), A semiempirical equatorial mapping of AMIE convection electric potentials (MACEP) for the January 10, 1997, magnetic storm, *J. Geophys. Res.*, *106*, 12,903.

Burch, J. L. (2000), IMAGE mission overview, *Space Sci. Rev.*, *91*, 1.

Carpenter, D. L. (1963), Whistler evidence of a "knee" in the magnetospheric ionization density profile, *J. Geophys. Res.*, *68*, 1675.

Carpenter, D. L., and R. R. Anderson (1992), An ISEE/whistler model of equatorial electron density in the magnetosphere, *J. Geophys. Res.*, *97*, 1097.

Chappell, C. R., K. K. Harris, and G. W. Sharp (1970), The morphology of the bulge region of the plasmasphere, *J. Geophys. Res.*, *75*, 3848.

Chen, A. J., and R. A. Wolf (1972), Effects on the plasmasphere of a time-varying convection electric field, *Planet. Space Sci.*, *20*, 483.

Chen, M. W., M. Schulz, G. Lu, and L. R. Lyons (2003), Quasi-steady drift paths in a model magnetosphere with AMIE electric field: Implications for ring current formation, *J. Geophys. Res.*, *108*(A5), 1180, doi:10.1029/2002JA009584.

Craven, P. D., D. L. Gallagher, and R. H. Comfort (1997), Relative concentration of He^+ in the inner magnetosphere as observed by the DE 1 retarding ion mass spectrometer, *J. Geophys. Res.*, *102*, 2279.

Dessler, A. J., and R. Karplus (1961), Some effects of diamagnetic ring currents on Van Allen radiation, *J. Geophys. Res.*, *66*, 2289.

Dessler, A. J., and E. N. Parker (1959), Hydromagnetic theory of geomagnetic storms, *J. Geophys. Res.*, *64*, 2239.

Ejiri, M. (1978), Trajectory traces of charged particles in the magnetosphere, *J. Geophys. Res.*, *83*, 4798.

Fok, M.-C., J. U. Kozyra, A. F. Nagy, C. E. Rasmussen, and G. V. Khazanov (1993), A decay model of equatorial ring current and the associated aeronomical consequences, *J. Geophys. Res.*, *98*, 19,381.

Fok, M.-C., R. A. Wolf, R. W. Spiro, and T. E. Moore (2001), Comprehensive computational model of the Earth's ring current, *J. Geophys. Res.*, *106*, 8417.

Fok, M.-C., et al. (2003), Global ENA image simulations, *Space Sci. Rev.*, *109*, 77.

Foster, J. C., and F. J. Rich (1998), Prompt midlatitude electric field effects during severe geomagnetic storms, *J. Geophys. Res.*, *103*, 26,367.

Foster, J. C., and H. B. Vo (2002), Average characteristics and activity dependence of the subauroral polarization stream, *J. Geophys. Res.*, *107*(A12), 1475, doi:10.1029/2002JA009409.

Foster, J. C., J. M. Holt, R. E. Musgrove, and D. S. Evans (1986), Ionospheric convection associated with discrete levels of particle precipitation, *Geophys. Res. Lett.*, *13*, 656.

Gallagher, D. L., P. D. Craven, R. H. Comfort, and T. E. Moore (1995), On the azimuthal variation of core plasma in the equatorial magnetosphere, *J. Geophys. Res.*, *100*, 23,597.

Gallagher, D. L., P. D. Craven, and R. H. Comfort (1998), A simple model of magnetospheric trough total density, *J. Geophys. Res.*, *103*, 9293.

Gallagher, D. L., P. D. Craven, and R. H. Comfort (2000), Global core plasma model, *J. Geophys. Res.*, *105*, 18,819.

Goldstein, J., R. W. Spiro, P. H. Reiff, R. A. Wolf, B. R. Sandel, J. W. Freeman, and R. L. Lambour (2002), IMF-driven overshielding electric field and the origin of the plasmaspheric shoulder on May 24, 2000, *Geophys. Res. Lett.*, *29*(16), 1819, doi:10.1029/2001GL014534.

Goldstein, J., B. R. Sandel, W. T. Forrester, and P. H. Reiff (2003), IMF-driven plasmasphere erosion of 10 July 2000, *Geophys. Res. Lett.*, *30*(3), 1146, doi:10.1029/2002GL016478.

Grebowsky, J. M., Y. Tulunay, and A. J. Chen (1974), Temporal variations in the dawn and dusk midlatitude trough and plasmapause position, *Planet. Space Sci.*, *22*, 1089.

Green, J. C., and M. G. Kivelson (2001), A tale of two theories: How the adiabatic response and ULF waves affect relativistic electrons, *J. Geophys. Res.*, *106*, 25,777.

Greenspan, M. E., and D. C. Hamilton (2000), A test of the Dessler-Parker-Sckopke relation during magnetic storms, *J. Geophys. Res.*, *105*, 5419.

Iijima, T., and T. A. Potemra (1976), The amplitude distribution of field-aligned currents at northern latitudes observed by TRIAD, *J. Geophys. Res.*, *81*, 2165.

Jordanova, V. K., L. M. Kistler, J. U. Kozyra, G. V. Khazanov, and A. F. Nagy (1996), Collisional losses of ring current ions, *J. Geophys. Res.*, *101*, 111.

Jordanova, V. K., L. M. Kistler, C. J. Farrugia, and R. B. Torbert (2001), Effects of inner magnetospheric convection on ring current dynamics: March 10–12, 1998, *J. Geophys. Res*, *106*, 29,705.

Kamide, Y., A. D. Richmond, and S. Matsushida (1981), Estimation of ionospheric electric fields, ionospheric currents, and field-aligned currents from ground magnetic records, *J. Geophys. Res.*, *86*, 801.

Kennel, C. F., and H. E. Petschek (1966), Limit on stably trapped particle fluxes, *J. Geophys. Res.*, *71*, 1.

Khazanov, G. V., M. W. Liemohn, T. S. Newman, M.-C. Fok, and R. W. Spiro (2003), Self-consistent magnetosphere-ionosphere coupling: Theoretical studies, *J. Geophys. Res.*, *108*(A3), 1122, doi:10.1029/2002JA009624.

Khazanov, G. V., M. W. Liemohn, T. S. Newman, M.-C. Fok, and A. J. Ridley (2004a), Magnetospheric convection electric field dynamics and stormtime particle energization: Case study of the magnetic storm of 4 May 1998, *Ann. Geophys*, *22*, 497–510.

Khazanov, G. V., M. W. Liemohn, M.-C. Fok, T. S. Newman, and A. J. Ridley (2004b), Stormtime particle energization with high temporal resolution AMIE potentials, *J. Geophys. Res.*, *109*, doi:10.1029/2003JA010186, in press.

Lambour, R. L., L. A. Weiss, R. C. Elphic, and M. F. Thomsen (1997), Global modeling of the plasmasphere following storm sudden commencements, *J. Geophys. Res.*, *102*, 24,351.

Liemohn, M. W. (2003), Yet another caveat to the Dessler-Parker-Sckopke relation, *J. Geophys. Res.*, *108*(A6), 1251, doi:10.1029/2003JA009839.

Liemohn, M. W., J. U. Kozyra, V. K. Jordanova, G. V. Khazanov, M. F. Thomsen, and T. E. Cayton (1999), Analysis of early phase ring current recovery mechanisms during geomagnetic storms, *Geophys. Res. Lett.*, *26*, 2845.

Liemohn, M. W., J. U. Kozyra, M. F. Thomsen, J. L. Roeder, G. Lu, J. E. Borovsky, and T. E. Cayton (2001a), Dominant role of the asymmetric ring current in producing the stormtime *Dst**, *J. Geophys. Res.*, *106*, 10,883.

Liemohn, M. W., J. U. Kozyra, C. R. Clauer, and A. J. Ridley (2001b), Computational analysis of the near-Earth magnetospheric current system, *J. Geophys. Res.*, *106*, 29,531.

Liemohn, M. W., J. U. Kozyra, M. R. Hairston, D. M. Weimer, G. Lu, A. J. Ridley, T. H. Zurbuchen, and R. M. Skoug (2002), Consequences of a saturated convection electric field on the ring current, *Geophys. Res. Lett.*, *29*(9), 1348, doi:10.1029/2001GL014270.

Lu, G., P. H. Reiff, M. R. Hairston, R. A. Heelis, and J. L. Karty (1989), Distribution of convection potential around the polar cap boundary as a function of the interplanetary magnetic field, *J. Geophys. Res.*, *94*, 13,447.

McComas, D. J., S. J. Bame, P. Barker, W. C. Feldman, J. L. Phillips, P. Riley, and J. W. Griffee (1998), Solar Wind Electron Proton Alpha Monitor (SWEPAM) for the Advanced Composition Explorer, *Space Sci. Rev.*, *86*, 563.

McIlwain, C. E. (1986), A *Kp* dependent equatorial electric field model, *Adv. Space Res.*, *6*(3), 187.

Ober, D. M., J. L. Horwitz, and D. L. Gallagher (1997), Formation of density troughs embedded in the outer plasmasphere by subauroral ion drift events, *J. Geophys. Res.*, *102*, 14,595.

Papitashvili, V. O., B. A. Belov, D. S. Faermark, Y. I. Feldstein, S. A. Golyshev, L. I. Gromova, and A. E. Levitin (1994), Electric potential patterns in the northern and southern polar regions parameterized by the interplanetary magnetic field, *J. Geophys. Res.*, *99*, 13,251.

Parker, E. N. (1957), Newtonian development of the dynamical properties of ionized gases of low density, *Phys. Rev.*, *107*, 924.

Parker, E. N., and H. A. Stewart (1967), Nonlinear inflation of a magnetic dipole, *J. Geophys. Res.*, *72*, 5287.

Rairden, R. L., L. A. Frank, and J. D. Craven (1986), Geocoronal imaging with Dynamics Explorer, *J. Geophys. Res.*, *91*, 13,613.

Rasmussen, C. E., S. M. Guiter, and S. G. Thomas (1993), Two-dimensional model of the plasmasphere: Refilling time constants, *Planet. Space Sci.*, *41*, 35.

Richmond, A. D., and Y. Kamide (1988), Mapping electrodynamic features of the high-latitude ionosphere from localized observations: Technique, *J. Geophys. Res.*, *93*, 5741.

Ridley, A. J., and M. W. Liemohn (2002), A model-derived description of the penetration electric field, *J. Geophys. Res.*, *107*(A8), 1151, doi:10.1029/2001JA00051.

Ridley, A. J., D. L. De Zeeuw, T. I. Gombosi, and K. G. Powell (2001), Using steady-state MHD results to predict the global state of the magnetosphere-ionosphere system, *J. Geophys. Res.*, *106*, 30,067.

Ridley, A. J., T. I Gombosi, and D. L. De Zeeuw (2004), Ionospheric control of the magnetosphere: Conductance, *Ann. Geophys*, *22*, 567–584.

Rowland, D. E., and J. R. Wygant (1998), Dependence of the large-scale inner magnetospheric electric field on geomagnetic activity, *J. Geophys. Res.*, *103*, 14,959.

Sandel, B. R., et al. (2000), The extreme ultraviolet imager investigation for the IMAGE mission, *Space Sci. Rev.*, *91*, 197.

Sandel, B. R., J. Goldstein, D. L. Gallagher, and M. Spasojevic (2003), Extreme ultraviolet imager observations of the structure and dynamics of the plasmasphere, *Space Sci. Rev.*, *109*, 197.

Sckopke, N. (1966), A general relation between the energy of trapped particles and the disturbance field near the Earth, *J. Geophys. Res.*, *71*, 3125.

Smith, C. W., M. H. Acuña, L. F. Burlaga, J. L'Heureux, N. F. Ness, and J. Scheifele (1998), The ACE magnetic fields experiment, *Space Sci. Rev.*, *86*, 613.

Sojka, J. J., C. E. Rasmussen, and R. W. Schunk (1986), An interplanetary magnetic field dependent model of the ionospheric convection electric field, *J. Geophys. Res.*, *91*, 11,281.

Southwood, D. J., and R. A. Wolf (1978), An assessment of the role of precipitation in magnetospheric convection, *J. Geophys. Res.*, *83*, 5227.

Spiro, R. W., and R. A. Wolf (1984), Electrodynamics of convection in the inner magnetosphere, in *Magnetospheric Currents*, *Geophys. Monogr. Ser.*, vol. 28, edited by T. A. Potemra, p. 247, AGU, Washington, D. C.

Stern, D. P. (1975), The motion of a proton in the equatorial magnetosphere, *J. Geophys. Res.*, *80*, 595.

Strobel, D. F., T. R. Young, R. R. Meier, T. P. Coffey, and A. W. Ali (1974), The nighttime ionosphere: *E* region and lower *F* region, *J. Geophys. Res.*, *79*, 3171.

Sugiura, M., and T. Kamei (1991), Equatorial *Dst* index 1957–1986, *IAGA Bull. 40*, Int. Assoc. of Geomagn. and Aeron., Saint-Maur-des-fosses, France.

Summers, D., R. M. Thorne, and F. Xiao (1998), Relativistic theory of wave-particle resonant diffusion with application to electron acceleration in the magnetosphere, *J. Geophys. Res.*, *103*, 20,487.

Tsyganenko, N. A., H. J. Singer, and J. C. Kasper (2003), Storm-time distortion of the inner magnetosphere: How severe can it get?, *J. Geophys. Res.*, *108*(A5), 1209, doi:10.1029/2002JA009808.

Volland, H. (1973), A semiempirical model of large-scale magnetospheric electric fields, *J. Geophys. Res.*, *78*, 171.

Weimer, D. R. (1996), A flexible, IMF dependent model of high-latitude electric potentials having "space weather" applications, *Geophys. Res. Lett.*, *23*, 2549.

Weimer, D. R. (1999), Substorm influence on the ionosphere electric potentials and currents, *J. Geophys. Res.*, *104*, 185.

Weiss, L. A., R. L. Lambour, R. C. Elphic, and M. F. Thomsen (1997), Study of plasmaspheric evolution using geosynchronous observations and global modeling, *Geophys. Res. Lett.*, *24*, 599.

Young, D. T., H. Balsiger, and J. Geiss (1982), Correlations of magnetospheric ion composition with geomagnetic and solar activity, *J. Geophys. Res.*, *87*, 9077.

D. L. Gallagher, National Space Science and Technology Center, NASA Marshall Space Flight Center, Huntsville, AL 35899, USA. (dennis.l.gallagher@nasa.gov)

J. U. Kozyra, M. W. Liemohn, and A. J. Ridley, University of Michigan, Atmospheric, Oceanic, and Space Sciences Department, 2455 Hayward Street, Ann Arbor, MI 48109-2143, USA. (jukozyra@umich.edu; liemohn@umich.edu; ridley@umich.edu)

D. M. Ober, Mission Research Corporation, 589 W. Hollis Street, Suite 201, Nashua, NH 03062, USA. (daniel.ober@mrcnh.com)